

Microscopic coexistence of superconductivity and magnetism in $\text{Ca}_{1-x}\text{Na}_x\text{Fe}_2\text{As}_2$

Philipp Materne,¹ Sirko Kamusella,¹ Rajib Sarkar,¹ Til Goltz,¹ Johannes Spehling,¹ Hemke Maeter,¹ Luminita Harnagea,² Sabine Wurmehl,^{1,2} Bernd Büchner,^{1,2} Hubertus Luetkens,³ Carsten Timm,⁴ and Hans-Henning Klauss¹

¹*Institute of Solid State Physics, TU Dresden, D-01069 Dresden, Germany*

²*Leibniz Institute for Solid State and Materials Research (IFW) Dresden, D-01069, , Germany*

³*Laboratory for Muon Spin Spectroscopy, Paul Scherrer Institute, CH-5232 Villigen, Switzerland*

⁴*Institute of Theoretical Physics, TU Dresden, D-01069 Dresden, Germany*

(Dated: August 14, 2018)

We present a detailed investigation of the magnetic and superconducting properties of $\text{Ca}_{1-x}\text{Na}_x\text{Fe}_2\text{As}_2$ single crystals with $x = 0.00, 0.35, 0.50$, and 0.67 by means of the local probe techniques Mössbauer spectroscopy and muon spin relaxation experiments. With increasing Na-substitution level, the magnetic order parameter as well as the magneto-structural phase transition are suppressed. For $x = 0.50$ we find a microscopic coexistence of magnetic and superconducting phases accompanied by a reduction of the magnetic order parameter below the superconducting transition temperature T_c . A systematic comparison with other 122 pnictides reveals a square-root correlation between the reduction of the magnetic order parameter and the ratio of the transition temperatures, T_c/T_N , which can be understood in the framework of a Landau theory. In the optimally doped sample with $T_c \approx 34$ K, diluted magnetism is found and the temperature dependence of the penetration depth and superfluid density are obtained, proving the presence of two superconducting s -wave gaps.

PACS numbers: 74.70.Xa, 76.75.+i, 76.80.+y, 74.62.Dh

I. INTRODUCTION

Since the discovery of superconductivity in iron pnictides,¹ their electronic phase diagrams, characterized by a close proximity of magnetic and superconducting phases, have been explored in great detail. Of particular interest are the regions of the phase diagrams showing a crossover from magnetic order to superconductivity. Magnetic spin fluctuations, enhanced in the vicinity of a magnetic quantum critical point, can play an important role in the formation of Cooper pairs. In addition, the interplay of both magnetic order and superconductivity can lead to a phase with microscopic coexistence of both ground states.^{2–6} As both states compete for the same electrons at the Fermi surface, the magnetic order parameter may be reduced below T_c .^{4–6} In this work, we studied the system $\text{Ca}_{1-x}\text{Na}_x\text{Fe}_2\text{As}_2$. The parent compound CaFe_2As_2 shows spin density wave order below the Néel-temperature $T_N = 165$ K.⁷ The magnetic phase transition is accompanied by a structural phase transition from a tetragonal to an orthorhombic structure.⁸ Increasing the Na amount in $\text{Ca}_{1-x}\text{Na}_x\text{Fe}_2\text{As}_2$, the magneto-structural phase transition is suppressed until it vanishes at a critical Na concentration $x \approx 0.35$.⁷ Superconductivity is found for $x \geq 0.3$ with a maximum of $T_c \approx 34$ K at an optimal doping of $x \approx 0.66$. However, the interaction of superconductivity with the magnetic spin density wave in the region of $0.3 \leq x \leq 0.35$ has not been conclusively determined.

We studied the magneto-structural phase transition as well as both the superconducting and the magnetic order parameter and their interaction for different Na-substitution levels. We find a suppression of the magneto-structural phase transition upon Na substitu-

tion. For $x = 0.35$ and 0.50 , microscopic coexistence of magnetic order and superconductivity is observed. For the latter Na-substitution level, a reduction of the magnetic order parameter is observed below the superconducting transition temperature. For $x = 0.67$, two superconducting gaps with s -wave symmetry can be deduced from the temperature dependence of the superfluid density.

II. EXPERIMENTAL

We examined mosaics of $\text{Ca}_{1-x}\text{Na}_x\text{Fe}_2\text{As}_2$ single crystals, which were grown by the self-flux technique as described by Johnsen *et al.*⁹ The samples were characterized by energy-dispersive X-ray spectroscopy (EDX), X-ray diffraction (XRD), susceptibility, magnetization, and specific-heat measurements. The stoichiometry of the examined samples is $x = 0.00, 0.35, 0.50$, and 0.67 as determined by EDX. A characterization of the magnetic properties was performed using SQUID magnetometry in large and small external magnetic fields. Mössbauer spectroscopy (MBS) experiments were performed in transmission geometry in a temperature range between 4.2 and 300 K using a CryoVac Konti IT cryostat. As the γ source, a ^{57}Co in rhodium matrix was used. The single crystals were aligned with the crystallographic c -axis along the γ direction. To analyze the data, the hyperfine Hamiltonian including electric quadrupole and magnetic hyperfine interactions was diagonalized. In the paramagnetic temperature regime, the spectra were described by a doublet pattern, whereas in the magnetically ordered state a sextet pattern was used. The magnetic order parameter is deduced from the ^{57}Fe magnetic hyperfine field

B_{hf} . The isomer shift δ is given with respect to α -Fe.

Muon spin relaxation (μ SR) experiments were performed at the π M3 and PiE1 beamlines of the Swiss Muon Source at the Paul Scherrer Institut, Switzerland, using the GPS and DOLLY spectrometers. The single crystals were aligned with the crystallographic c -axis along the muon beam. Positively charged muons μ^+ , which are nearly 100% spin-polarized due to parity violation during the pion decay, are implanted in the sample and thermalize at interstitial lattice sites, where they radioactively decay with a lifetime of 2.2 μ s into two neutrinos and one positron. As the muon decay involves the weak interaction, where parity conservation is violated, the positron is predominately emitted along the direction of the muon spin at the moment of the decay. Measuring the time-resolved angular distribution of the emitted positrons allows to extract the time evolution of the muon spin polarization $P(t)$. The initial muon spin was rotated by approximately -45° with respect to the beam, which allows to measure the time evolution of the muon spin polarization $\perp c$ and $\parallel c$ by analysing the asymmetry of the up-down and forward-backward detector pair respectively. If not stated otherwise, all presented measurements refer to the up-down detector pair. The muon spin relaxation was measured for temperatures ranging from 1.6 K up to 300 K in zero field (ZF) and transverse magnetic fields (TF) up to 130 mT. The μ SR data were analyzed using the MUSRFIT software package.¹⁰

In a magnetically ordered material, the muon spin exhibits a Larmor precession with a frequency ν_μ , which is related to the local magnetic field B at the muon site by $\nu_\mu = B\gamma_\mu/(2\pi)$ (muon gyromagnetic ratio $\gamma_\mu = 2\pi \times 135.5$ MHz/T). The muon spin precession can be described in single crystals using the function¹¹

$$P(t) = \sum_{i=1}^N P(\nu_i) \left[A_i \cos(\nu_i t) e^{-\lambda_T^i t} + (1 - A_i) e^{-\lambda_L^i t} \right], \quad (1)$$

with N denoting the number of inequivalent muon sites contributing to the μ SR signal, weighted by $P(\nu_i)$. In the case of 100% magnetic ordering, $\sum P(\nu_i) = 1$. A_i describes the oscillating part of the signal. In contrast to powder samples, where $A_i = 2/3$ due to spatial averaging, for single crystals $A_i \in [0, 1]$. λ_T , describing the damping of the oscillation, is a measure of the width of the static field distribution, also including dynamic contributions due to magnetic fluctuations. The damping of the non-oscillating part, described by λ_L , is caused by dynamic magnetic fluctuations only.¹²

To study the superconducting properties of the sample with μ SR, a magnetic field $\mu_0 H_{\text{ext}}$ was applied parallel or perpendicular to the muon beam. In type-II superconductors, a vortex lattice is formed for $\mu_0 H_{c1} < \mu_0 H_{\text{ext}} < \mu_0 H_{c2}$ resulting in a spatial magnetic field distribution.¹³ This magnetic field distribution causes an additional damping of the muon spin os-

cillation, which can be modeled via additional Gaussian terms of the form¹³

$$P(t) = \sum_{i=1}^N \left[P_i \cos(\gamma_\mu B_i t + \varphi) e^{-\frac{1}{2}\sigma_i^2 t^2} \right] e^{-\frac{1}{2}\sigma_N^2 t^2}, \quad (2)$$

where σ_i describes the damping due to superconductivity, σ_N the damping due to nuclear magnetic dipole contributions and φ denotes the angle between the initial muon spin direction and the positron detector.

The second moment $\langle \Delta B^2 \rangle$ of the internal magnetic field distribution, $n(B)$, is given by¹³

$$\langle \Delta B^2 \rangle = \sum_{i=1}^N \frac{A_i}{\sum_{i=1}^N A_i} \left[\left(\frac{\sigma_i}{\gamma_\mu} \right)^2 + (B_i - \langle B \rangle)^2 \right] \quad (3)$$

and related to the London penetration depths λ by the relation¹⁴

$$\langle \Delta B^2 \rangle = 0.00371 \Phi_0^2 \frac{1}{\lambda^4}, \quad (4)$$

where Φ_0 denotes the magnetic flux quantum. λ is related to the Cooper pair density by $n_s \propto 1/\lambda^2$.

Therefore, μ SR allows to independently measure the magnetic and superconducting order parameters via the determination of the zero field muon spin precession frequency ν_i and the London penetration depth, respectively. Moreover, μ SR is able to distinguish between non-magnetic and magnetic volume fractions in the sample.

III. RESULTS AND DISCUSSION

Measurements of the magnetic susceptibility of CaFe_2As_2 are reported by Harnagea *et al.*¹⁵ Magnetic susceptibility measurements in an applied field of 1 T parallel to the ab -plane are shown in Fig. 1. For $x = 0.35$, 0.50, and 0.67 a nearly linear decrease of the magnetic susceptibility is observed in the paramagnetic region, which is found also for many other iron pnictides.^{16–18} The kink at 143 K, 119 K, and 150 K for $x = 0.35$, 0.50, and 0.67, respectively, indicates the onset of the antiferromagnetic (AFM) ordering. Magnetic susceptibility measurements in an applied field of 2 mT parallel to the ab -plane are shown in Fig. 2. For $x = 0.35$, below 17 K a broad superconducting transition occurs. As the diamagnetic shielding is not fully developed, only parts of the sample show superconductivity. For $x = 0.50$, a two-step superconducting transition occurs. Below 34 K, a slightly negative magnetic susceptibility is measured, which indicates a superconducting phase in a small volume of the sample. Below 17 K, a broad second transition occurs, where bulk superconductivity is formed resulting in the full superconducting response. For the further treatment of the $x = 0.50$ sample, 17 K will be considered as the superconducting transition temperature. This two-step behavior as well as the broad transition indicates an in-

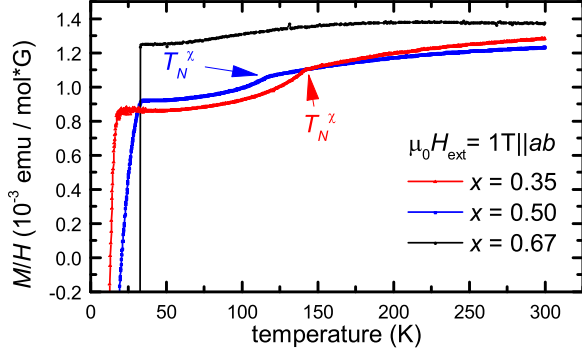


FIG. 1. Temperature dependence of the static susceptibility $\chi = M/H$ of $\text{Ca}_{1-x}\text{Na}_x\text{Fe}_2\text{As}_2$ for $x = 0.35, 0.50$, and 0.67 . The measurements were performed at an applied field of 1 T parallel to the ab -plane. T_N^x denotes the magnetic transition temperature.

homogeneous sample. The sample with $x = 0.67$ shows bulk superconductivity below 34 K. The sharp transition indicates a homogeneous sample.

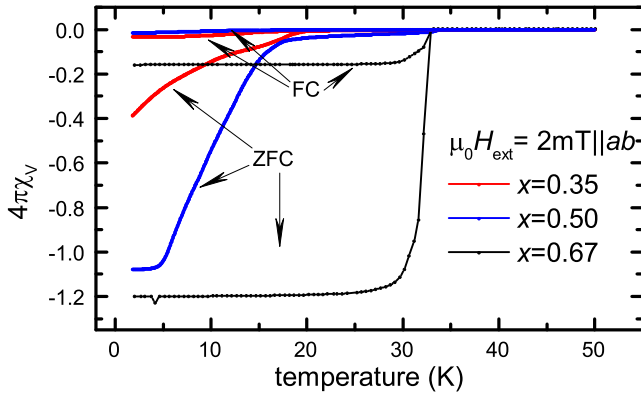


FIG. 2. Temperature dependence of the magnetic susceptibility χ_v [zero (ZFC) and field cooled (FC)] of $\text{Ca}_{1-x}\text{Na}_x\text{Fe}_2\text{As}_2$ for $x = 0.35, 0.50$, and 0.67 . The measurements were performed at an applied field of 2 mT parallel to the ab -plane.

A. The parent compound CaFe_2As_2

The time evolution of the muon spin polarization in ZF is shown in Fig. 3. In the paramagnetic temperature regime, a weak Gauss-Kubo-Toyabe damping of the signal is observed caused by the dipole-dipole interaction of the muon magnetic moment with randomly oriented nuclear magnetic moments. The temperature dependence of the magnetic volume fraction (MVF) is shown in Fig. 4. To describe MVF as a function of T , two temperatures are defined: T_N^{onset} describes the highest temperature with a finite MVF and $T_N^{100\%}$ describes the highest temperatures with $\text{MVF} = 100\% \hat{=} 1$.

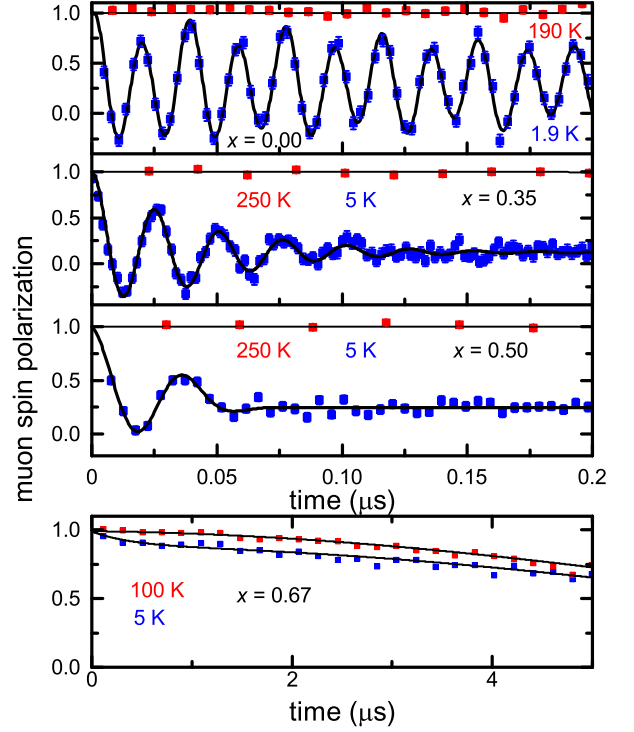


FIG. 3. ZF- μ SR time spectra of $\text{Ca}_{1-x}\text{Na}_x\text{Fe}_2\text{As}_2$ for characteristic temperatures in the paramagnetic and magnetically ordered state. The well-defined muon spin precession for $x = 0.00, 0.35$, and 0.50 indicate long-range commensurate magnetic order. For $x = 0.67$, non-magnetic behavior is found down to lowest measured temperatures.

The sharp transition between $T_N^{\text{onset}} = 167$ K and $T_N^{100\%} = 163$ K indicates a homogeneous sample. Below 167 K, two magnetically inequivalent muon stopping sites A and B with a temperature-independent occupation ratio of $P_A:P_B = 80:20$ were observed as it was found in BaFe_2As_2 .¹⁹ The signal fraction corresponding to muons stopping at site A show a well-defined sinusoidal oscillation below 167 K. This indicates static long-range commensurate magnetic order. The temperature dependence of ν_A is shown in Fig. 5. The step-like behavior indicate a first-order transition, as it was seen in SrFe_2As_2 .²⁰ The signal fraction corresponding to muons stopping at site B show an exponential relaxation below 167 K and a well-defined sinusoidal oscillation below 60 K. This indicates a broad field distribution at temperatures between 60 K and 167 K at the muon stopping site B suppressing a coherent oscillation of the muon spins, which is contrary to the observations in BaFe_2As_2 , where the two oscillation frequencies were obtained at all temperatures below T_N ,¹⁹ but consistent with LaOFeAs .²¹ Below 60 K, the two precession frequencies have a temperature-independent ratio of $\nu_A/\nu_B \approx 1.9$. Therefore, the magnetic field at the muon stopping site A is higher than on site B . Site A is located next to the FeAs -layer.²² The smaller value of the magnetic field at site B indicates

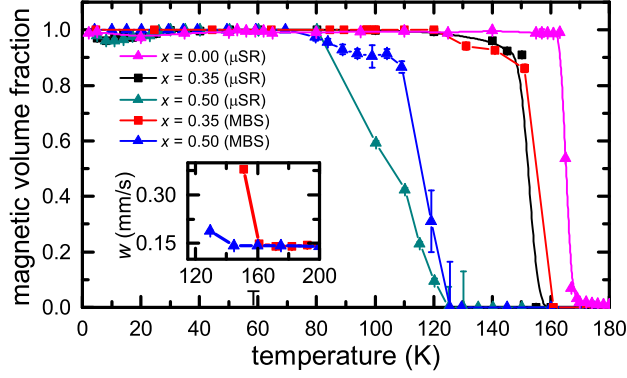


FIG. 4. Magnetic volume fraction as a function of temperature (lines are guides to the eye only) of $\text{Ca}_{1-x}\text{Na}_x\text{Fe}_2\text{As}_2$ obtained from ZF- μSR and Mössbauer spectroscopy for $x = 0.00, 0.35$, and 0.50 . The inset shows the temperature dependence of the Mössbauer linewidth w . The abrupt increase of w indicates magnetic ordering.

a muon stopping site more distant from the FeAs layer. As the precession frequency is proportional to the magnetic field at the muon site, this ratio is different from BaFe_2As_2 ²³ and SrFe_2As_2 ,²⁰ showing ratios of 4.1 and 3.4. The ionic radii of the alkaline earth metals scale like $\text{Ca} < \text{Sr} < \text{Ba}$.²⁴ As a consequence, the crystallographic c -axis is shortest for CaFe_2As_2 ⁷ and longest for BaFe_2As_2 .²⁵ By shrinking the crystallographic c -axis, the distance between site B and the ordered iron magnetic moments in the FeAs-layer is reduced. The muon spin interacts with the ordered electronic moments via dipole-dipole and transferred Fermi-contact interaction. Both interactions are sensitive to the distance between the muon spin and the iron ordered moments. This implies that the change of the frequency ratio in the undoped compounds has a structural origin.

Mössbauer measurements by Alzamora *et al.*²⁶ on CaFe_2As_2 show a first-order-like magneto-structural phase transition below 173 K. They report a saturated magnetic hyperfine field of ≈ 10.1 T at 4.2 K. The angle between the magnetic hyperfine field and the principal axis of the electric field gradient was reported as $94(4)^\circ$. Therefore, as the principal axis of the electric field gradient is parallel to the crystallographic c -axis,²⁶ the magnetic hyperfine field is located in the ab -plane.^{26,27} These Mössbauer results are consistent with our μSR results showing that the magnetic moments are located in the ab -plane.

B. Underdoped $\text{Ca}_{0.65}\text{Na}_{0.35}\text{Fe}_2\text{As}_2$ and $\text{Ca}_{0.50}\text{Na}_{0.50}\text{Fe}_2\text{As}_2$

Mössbauer spectra for characteristic temperatures in the paramagnetic and magnetically ordered states are shown in Fig. 6. In the paramagnetic state, an asym-

metric doublet structure, which is caused by the interaction of the nucleus with an electric field gradient (EFG), was observed for both stoichiometries. However, in the principal-axis system, the EFG is fully determined by its z -component V_{zz} and the asymmetry parameter η (which turned out to be zero for all investigated temperatures). At room temperature, for $x = 0.35$ and 0.50 a value of $V_{zz} = 11.2(5)$ V/Å² was obtained. With decreasing temperature, V_{zz} slightly increases to $13.0(5)$ V/Å² directly above the magnetic transition temperature as shown in Fig. 7. With the onset of magnetic order, V_{zz} increases to $19(2)$ V/Å² and $18(3)$ V/Å² for $x = 0.35$ and 0.50 , respectively, and remains constants within error bars down to lowest temperature. This increase can be assigned to a magneto-structural phase transition as observed for other 122 compounds.^{28,29} Furthermore, the principal axis of the EFG is parallel to the crystallographic c -axis. The temperature dependence of the angle θ between the principal axis of the EFG and the magnetic hyperfine field, obtained from a fit to the data, is shown in Fig. 7. We have obtained $\theta = 80(5)^\circ$ and $71(5)^\circ$ for $x = 0.35$ and 0.50 , respectively, in the fully ordered state were obtained. These values indicate a tilting of the magnetic moments out of the ab -plane.

The time evolution of the muon spin polarization in ZF on $\text{Ca}_{1-x}\text{Na}_x\text{Fe}_2\text{As}_2$ (with $x = 0.00, 0.35, 0.50$, and 0.67) is shown in Fig. 3. As for the parent compound described above, a weak Gauss-Kubo-Toyabe damping of the signal is observed caused by the dipole-dipole interaction of the muon magnetic moment with randomly oriented nuclear magnetic moments in the paramagnetic temperature regime. The onset of long-range commensurate magnetic ordering below $T_N^{\text{onset}} = 160(2)$ K and $125(3)$ K for $x = 0.35$ and 0.50 , respectively, is indicated by the appearance of a well-defined muon spin precession with two frequencies ν_A and ν_B . The occupation probability is independent of temperature and the Na-substitution level ($P(\nu_A):P(\nu_B) = 80:20$). We conclude that two magnetically inequivalent muon sites are present in a homogeneous magnetically ordered phase. The temperature dependence of the muon frequency ν_A for both samples is shown in Fig. 5(a) and 5(b). The onset temperature is consistent with the results of the macroscopic magnetizations measurements by SQUID magnetometry. The two frequencies have a temperature-independent ratio of $\nu_A/\nu_B \approx 4$ and 8 for $x = 0.35$ and 0.50 , respectively, which are different compared to the undoped compound showing $\nu_A/\nu_B \approx 1.9$. This change is more drastic compared to other 122 compounds. BaFe_2As_2 shows a ratio of 4.1,²³ which increases to 4.47 for $\text{Ba}_{0.77}\text{K}_{0.23}\text{Fe}_2\text{As}_2$ ²³ and 4.5 for $\text{Ba}_{0.7}\text{Na}_{0.3}\text{Fe}_2\text{As}_2$.³⁰ SrFe_2As_2 shows a ratio of 3.4,²⁰ which changes to 3.6 for $\text{Sr}_{0.5}\text{Na}_{0.5}\text{Fe}_2\text{As}_2$.³¹ Substituting an alkaline-earth metal by an alkaline metal with a smaller ionic radius ($\text{Ba} \rightarrow \text{Na}$, $\text{Sr} \rightarrow \text{Na}$), leads to a smaller change in the c -axis parameter and the change of the precession frequency ratio ν_A/ν_B occurs at lower substitution levels than by substituting with an alkaline metal with a larger ionic ra-

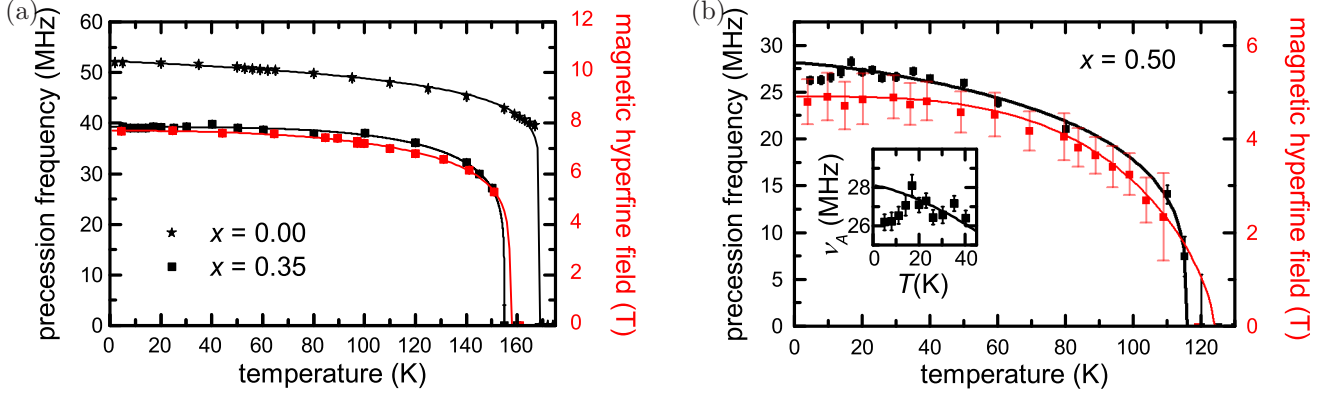


FIG. 5. Temperature dependence of the magnetic order parameter for (a) $x = 0.00$ and 0.35 and (b) $x = 0.50$ including best order parameter fits according to Eq. (5). The magnetic hyperfine field for $x = 0.50$ is Gaussian-distributed. The average value of the Gaussian distribution is shown with one standard deviation as error bar. The inset in (b) shows the low temperature regime, where superconductivity occurs below $T_c = 17$ K.

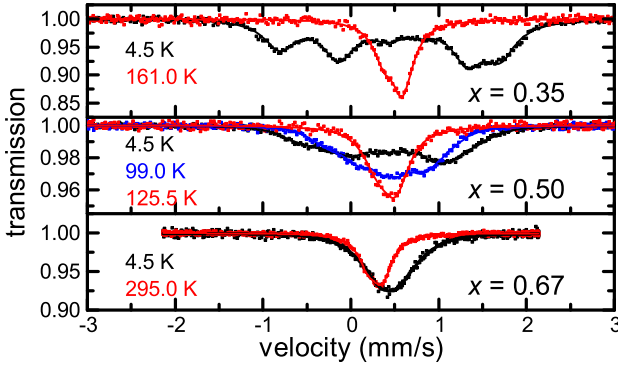


FIG. 6. Mössbauer spectra of $\text{Ca}_{1-x}\text{Na}_x\text{Fe}_2\text{As}_2$ for characteristic temperatures in the paramagnetic and magnetically ordered state. The sextet structure of the Mössbauer spectra for $x = 0.35$ and 0.50 indicate long-range commensurate magnetic order. For $x = 0.67$, a broadening below ≈ 150 K is observed, which cannot be described by a change in V_{zz} indicating small magnetic fields at the iron nucleus.

dius ($\text{Ca} \rightarrow \text{Na}$, $\text{Ba} \rightarrow \text{K}$, $\text{Sr} \rightarrow \text{K}$).^{7,20,25,30–33} The ionic radii scale like $\text{Ca} < \text{Na} < \text{Sr} < \text{Ba} < \text{K}$.²⁴ By increasing the Na-substitution level in $\text{Ca}_{1-x}\text{Na}_x\text{Fe}_2\text{As}_2$, the crystallographic c -axis is elongated resulting in an increased distance of the muon spin at the site B from the iron ordered moments in the FeAs -plane. In addition, the small tilting of the magnetic moments out of the ab -plane may also change the magnetic field at the muon site. However, a change in the Fermi-contact interaction for both muon stopping sites cannot be ruled out. Additionally, a signal fraction in the forward-backward detector pair (not shown here) showing an exponential relaxation is observed in the magnetically ordered phase. This signal fraction increases as a function of Na-substitution level. This is consistent with the tilting of the magnetic moments out of the ab -plane as observed by Mössbauer

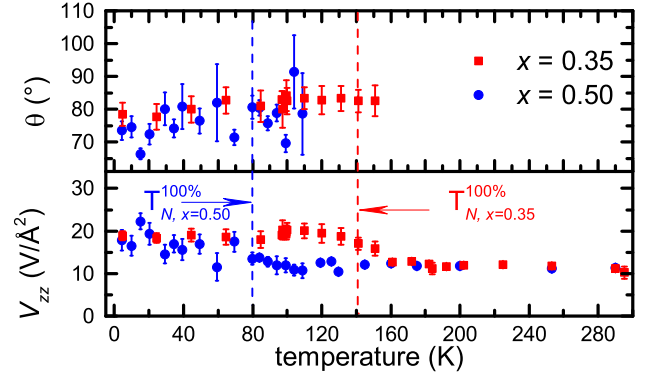


FIG. 7. Temperature dependence of θ , the polar angle between the magnetic hyperfine field B_{hf} and the principal axis of the electric field gradient, V_{zz} . The increase of V_{zz} indicates a change in the electromagnetic environment of the ^{57}Fe -nucleus and corresponds to the magneto-structural phase transition. The vertical dashed lines denotes the highest temperature, where the samples shows a MVF of 100 %.

spectroscopy.

The temperature dependence of the magnetic volume fraction was determined independently by ZF- and TF- μSR measurements as well as Mössbauer spectroscopy. TF- μSR experiments were performed by applying a magnetic field of 5 mT perpendicular to the initial muon spin polarization. The temperature dependence of the MVF is shown in Fig. 4. The onset of the magnetic ordering is also indicated by the abrupt increase of the Mössbauer line width w due to appearance of a magnetic hyperfine field. This increase is shown in the inset of Fig. 4 leading to $T_{\text{onset}} = 161(2)$ K and $125(3)$ K for $x = 0.35$ and 0.50 , respectively. Therefore, the obtained characteristic temperatures of the magnetic phase transition are of equal value within error bars for both μSR and MBS and coincide with the magnetic phase transition

temperature obtained by magnetic susceptibility measurements, T_N^x . The temperature width of the phase transition, $\Delta T = T_N^{\text{onset}} - T_N^{100\%}$, increased from 4 K to 21 K and 45 K for $x = 0.00$, 0.35, and 0.50, respectively. We attribute this increased width of the magnetic phase transition to the increased degree of disorder due to the Na-substitution. The MVF is constant below $T_N^{100\%} = 163(2)$ K, 140(3)K and 80(3)K for $x = 0.00$, 0.35, and 0.50, respectively, proving bulk magnetic order. In the magnetically ordered state, a well-resolved sextet was observed in the Mössbauer spectra for $x = 0.35$, as it is shown in Fig. 6 at $T = 4.5$ K. This proves a static commensurate magnetic ground state with a well-defined hyperfine field. For $x = 0.50$, the sextet is less clearly resolved and the spectra were modeled using a Gaussian distribution of magnetic hyperfine fields. This takes into account a higher degree of disorder than in the sample with $x = 0.35$. Consistently also the μ SR transverse relaxation rate λ^T is largest for $x = 0.50$ as can be seen by a much faster suppression of the ZF oscillation in Fig. 3 compared to lower Na-substitution levels. The temperature dependence of the obtained magnetic hyperfine field of $x = 0.35$ is shown in Fig. 5a. The temperature dependence of the mean value of the obtained Gaussian distributed magnetic hyperfine field B_{hf} for $x = 0.50$ is shown in Fig. 5b.

Both ν_A and B_{hf} were analyzed using a fit to the temperature-dependent order parameter (M) of the form

$$M(T) = M(T = 0) \left[1 - \left(\frac{T}{T_N} \right)^\alpha \right]^\beta \quad (5)$$

for $x = 0.35$ and 0.50, respectively, above the superconducting transition temperatures (17 K in both cases). For $x = 0.35$, a fit to Eq.(5) above T_c for both $\nu_A(T)$ and $B_{\text{hf}}(T)$ represents the data in the whole temperature range, i.e., also below the superconducting transition. Therefore, no interaction between the magnetic and superconducting order parameter is detectable. For $x = 0.50$, the muon frequency is reduced by approximately 7 % below 17 K while the magnetic hyperfine field shows no reduction and is well-represented by Eq.(5). This reduction of the muon precession frequency proves the microscopic coexistence of magnetic order and superconductivity and their competition. Possibly $B_{\text{hf}}(T)$ shows no signatures for a reduction below 17 K, since the reduction of 7 % is within the hyperfine field error bars. Alternatively, the muon precession frequency may be reduced due to a spin reorientation below T_c rather than a reduction of the magnetic order parameter. However, in this scenario the angle θ between the magnetic hyperfine field B_{hf} and the principal axis of the EFG would change. The temperature dependence of θ is shown in Fig. 7. Since there is no systematic change of θ below T_c observed within error bars, a significant spin reorientation can be ruled out. Both order parameters are weakly coupled compared to $\text{Ba}_{1-x}\text{Na}_x\text{Fe}_2\text{As}_2$,³⁰ where a reduction of the muon spin precession frequency and therefore of

the magnetic order parameter of $\approx 65\%$ appears.

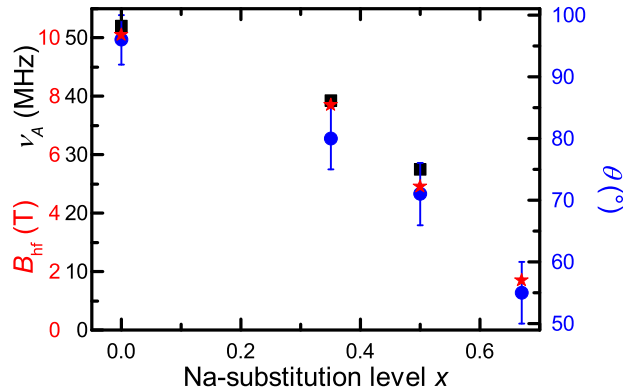


FIG. 8. Low-temperature saturation values of the magnetic hyperfine field B_{hf} , the muon spin precession frequency ν_A and θ , the angle between B_{hf} and the principal-axis of the EFG, as a function of the Na-substitution level. Upon Na substitution, a reduction of the magnetic hyperfine field and the muon spin precession frequency is observed proving a reduction of the magnetic order parameter. The decrease θ indicate a tilting of the magnetic moments out of the ab -plane as a function of the Na-substitution level.

C. Landau theory for coupled order parameters

In the case of coexistence of magnetic order and superconductivity, an interaction between both order parameters is expected to be present. This may change the magnitude of the order parameters and alter the critical temperatures with respect to the decoupled situation. We used a Landau theory to describe the coupling between the superconducting order parameter $\psi(\vec{r})$ and the magnetic order parameter $\vec{M}(\vec{r})$ in the case of coexistence and to describe the dependence of the reduction of the magnetic order parameter on the critical temperatures. The homogeneous free-energy functional in the absence of an external field is given by^{4,34–36}

$$F[\psi, \vec{M}] = \int d^3r \left[\frac{\alpha}{2} |\psi(\vec{r})|^2 + \frac{\beta}{4} |\psi(\vec{r})|^4 + \frac{a}{2} |\vec{M}(\vec{r})|^2 + \frac{b}{4} |\vec{M}(\vec{r})|^4 + \frac{d}{2} |\psi(\vec{r})|^2 |\vec{M}(\vec{r})|^2 \right], \quad (6)$$

where the coupling between of the two order parameters is contained in the last term. Following the common approach, α and a are described as

$$a = a_0(T - T_{N0}), \quad (7)$$

$$\alpha = \alpha_0(T - T_{c0}), \quad (8)$$

where T_{N0} and T_{c0} denote the bare magnetic and superconducting transition temperatures, respectively. The

bare transition temperatures describe the decoupled case. To ensure that the free-energy has a minimum and an that the two order parameters compete with each other, $\beta > 0$, $b > 0$, and $d > 0$ are required. The two order parameters are obtained by minimizing the free-energy functional $F[\psi, \vec{M}]$. The order parameters in the coexistence region are then given by

$$|\psi|^2 = -\frac{\alpha b - ad}{b\beta - d^2}, \quad \alpha b - ad < 0, \quad (9)$$

$$|\vec{M}|^2 = -\frac{a\beta - \alpha d}{b\beta - d^2}, \quad a\beta - \alpha d < 0. \quad (10)$$

This solution is stable for a sufficiently small coupling d , which satisfies $b\beta - d^2 > 0$. For the further treatment, $T_{c0} < T_{N0}$ is assumed, which is the case for sufficiently low doping in the 122 compounds. This results in $T_{N0} = T_N$. At T_c , where $|\psi|^2 = 0$, Eq. (9) reduces to

$$|\psi(T_c)|^2 = 0 = \alpha_0 b(T_c - T_{c0}) - a_0 d(T_c - T_N) \quad (11)$$

which results in a linear relation between the measured and bare superconducting transition temperatures. The temperature dependence of the magnetic order parameter in the coexistence regime is then given by

$$\begin{aligned} \vec{M}_{co}^2(T) = \frac{1}{b\beta - d^2} & \left\{ [\alpha_0 d - a_0 \beta] T \right. \\ & \left. + \left[a_0 \beta - \frac{a_0}{b} d^2 \right] T_N - \left[1 - \frac{a_0 d}{\alpha_0 b} \right] T_c \right\}. \end{aligned} \quad (12)$$

To investigate the reduction of the magnetic order parameter below the superconducting transition temperature, the ratio of $|\vec{M}_{co}|^2(T)$ and $|\vec{M}_0|^2(T) = a_0(T_N - T)/b$ for $T < T_c$ is calculated. The reduction is maximal for $T \rightarrow 0$. The ratio is then given by

$$\frac{\vec{M}_{co}^2}{\vec{M}_0^2}(T=0) = 1 - \frac{d}{a_0} \frac{\alpha_0 b - a_0 d}{b\beta - d^2} \frac{T_c}{T_N}. \quad (13)$$

Literature data for $|\vec{M}_{co}|^2/|\vec{M}_0|^2(T=0)$ as a function of T_c/T_N for various 122 compounds, measured by neutron scattering and μ SR, are shown in Fig. 9.^{23,30,37–46} In addition, the reduction of the structural order parameter $S = (a - b)/(a + b)$ is plotted in Fig. 9. The magnetic and structural order parameters show the same behavior, as they are strongly coupled in the 122 pnictides.^{20,27,29,47–51} $|\vec{M}_{co}|^2/|\vec{M}_0|^2(T=0)$ shows a nearly linear decrease as a function of T_c/T_N and hence the reduction of the magnetic order parameter shows a square root behavior. This corresponds to a constant slope in Eq. (13), which implies a similar coupling strength of the magnetic and superconducting order parameters in the 122 compounds. For $T_c/T_N \ll 1$, experimental data show no reduction of the magnetic order parameter in the coexistence regime. This may result from the fact that the samples show SC only in

parts of the sample volume, which has been observed for, e.g., $\text{Ca}_{0.65}\text{Na}_{0.35}\text{Fe}_2\text{As}_2$. Equation (13) qualitatively describes the reduction of $|\vec{M}_{co}|^2/|\vec{M}_0|^2(T=0)$ with increasing T_c/T_N ratio for $0 < T_c/T_N < 0.7$. The systematic deviations for $T_c/T_N > 0.7$ indicate an increase in the coupling strength. This means that the coupling is more effective if $T_c \approx T_N$.

D. Magneto-structural phase transition

The lattice dynamics of $\text{Ca}_{1-x}\text{Na}_x\text{Fe}_2\text{As}_2$ was investigated by analysing the temperature dependence of the Mössbauer-Lamb factor. The recoilless fraction f was extracted from the Mössbauer spectra using the absorption area method.⁵² In the Debye-approximation,⁵³

$$f \propto \exp \left\{ -\frac{3E_R}{2k_B\theta_D} \left[1 + 4 \left(\frac{T}{\theta_D} \right)^2 \int_0^{\theta_D/T} \frac{x}{e^x - 1} dx \right] \right\}, \quad (14)$$

with Boltzmann constant k_B , Debye temperature θ_D and the recoil energy E_R . The temperature dependence of the relative recoilless fraction $f(T)/f(4.2 \text{ K})$ is shown in Fig. 10. The data for temperatures above and below the phase transition were analyzed using Eq. (14) to investigate the influence of the magneto-structural transition on f . We accordingly define Debye temperatures θ_D^{PM} and θ_D^{AFM} . The step at 151 K for $x = 0.35$ and the gradual increase between 60 K and 125 K for $x = 0.50$ are attributed to an effective absorber-thickness effect. The magnetic phase transition leads to an increase of the absorption area compared to the paramagnetic region, due to a splitting of the resonance lines.^{53,54} The obtained Debye temperatures are shown in Tab. I. As the

x	$\theta_D^{\text{PM}}/\text{K}$	$\theta_D^{\text{AFM}}/\text{K}$
0.00	272 ⁵⁵	271 ⁵⁵
0.35	200(32)	208(16)
0.50	203(12)	219(28)
0.67	213(6)	

TABLE I. Debye temperatures θ_D obtained using Eq. (14) above (PM) and below (AFM) the magnetic phase transition.

Debye temperatures θ_D^{PM} and θ_D^{AFM} does not change significantly within error bars at the phase transition, we conclude that the lattice dynamics do not change upon the magneto-structural phase transition. Also, the obtained Debye temperatures are constant within error bars for all x . Therefore, the lattice dynamics are independent of the Na-substitution level in the investigated substitution range $0.35 \leq x \leq 0.67$. In comparison with the

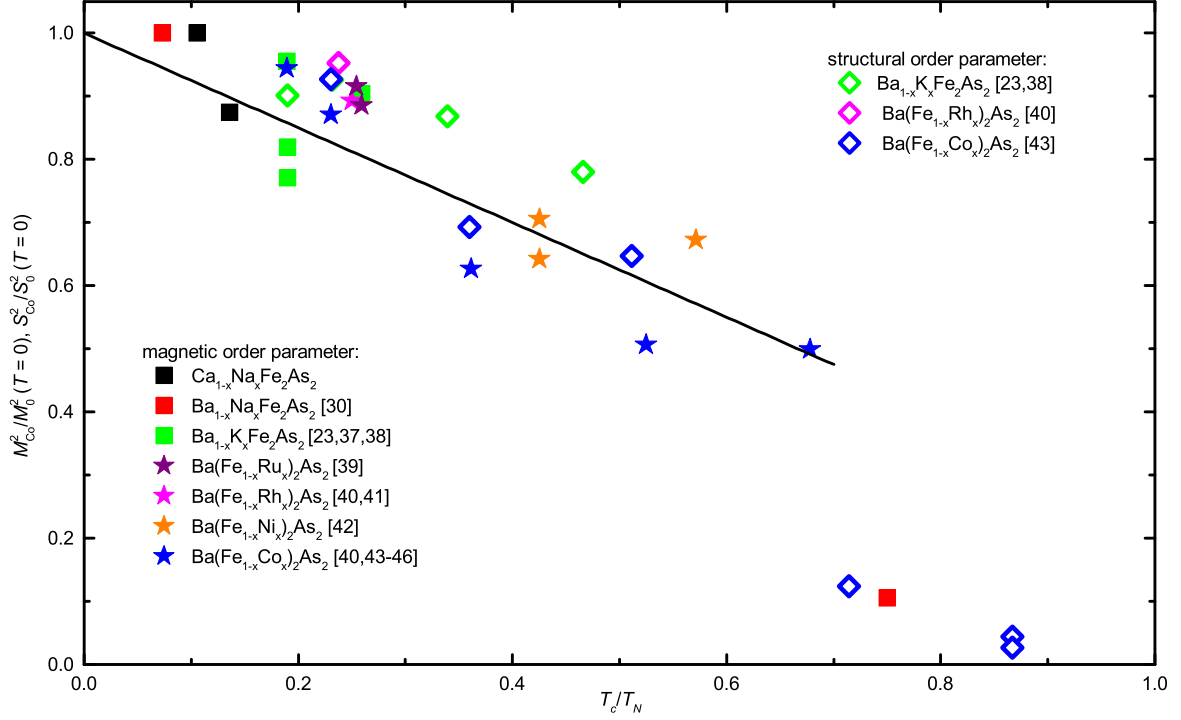


FIG. 9. $|\vec{M}_{\text{co}}|^2/|\vec{M}_0|^2(T=0)$ as a function of T_c/T_N for various 122 compounds.^{23,30,37-46} $|\vec{M}_{\text{co}}|^2$ denotes the magnetic order parameter in the region of coexistence with superconductivity. $|\vec{M}_0|^2$ denotes the magnetic order parameter without any superconductivity. The reduction of the magnetic order parameter in the coexistence region increases with increase of T_c/T_N following Eq. (13), the best linear fit for $T < 0.7$ is shown as the solid line.

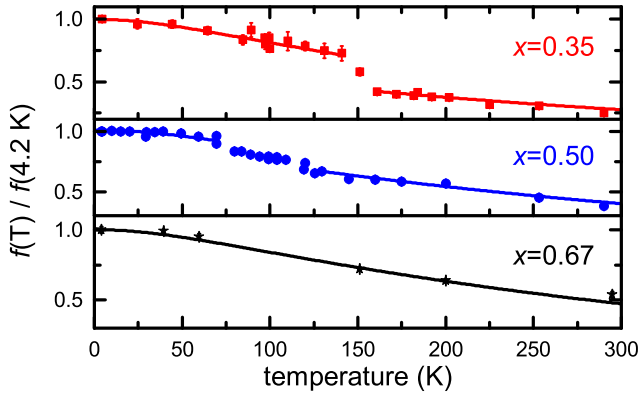


FIG. 10. Temperature dependence of the relative recoilless fraction $f(T)/f(4.2 \text{ K})$ including fits following Eq. 14.

undoped compound CaFe_2As_2 with $\theta_D^{x=0} \approx 270 \text{ K}$,⁵⁵ the lattice is softened considerably.

To further study the magnetic properties at the magneto-structural phase transition, the temperature dependence of the isomer shift δ was analyzed. δ is a measure for the electron density at the Fe-nucleus. The temperature dependence of the isomer shift,⁵³ which is shown in Fig. 11, is a sum of the temperature-independent chemical shift δ_C and a temperature dependent contri-

bution $\delta_R(T)$ due to the second-order Doppler shift

$$\delta(T) = \delta_C + \delta_R(T), \quad (15)$$

$$\delta_R(T) = -\frac{9}{16} \frac{k_B}{M_{\text{eff}} c} \left[\theta_D + 8T \left(\frac{T}{\theta_D} \right)^3 \int_0^{\theta_D/T} \frac{x^3}{e^x - 1} dx \right], \quad (16)$$

where M_{eff} denotes the effective mass of the ^{57}Fe atom. δ_C can be calculated using $\delta_C = \delta(0) - \delta_R(0)$. To study the influence of the magneto-structural phase transition on the isomer shift, the temperature dependence of the isomer shift was analyzed in the following way: $\delta(T)$ was analyzed in the paramagnetic state with a fixed θ_D , obtained from Eq. (14). Then, we extracted the temperature dependence from $\delta^{\text{PM}}(T)$. In a third step we have checked whether $\delta^{\text{PM}}(T)$ can describe the temperature dependence of the isomer shift in the magnetically ordered state or whether systematic deviations from the behavior in the paramagnetic state occur. $\delta^{\text{PM}}(T)$ reveals similar behavior for both samples with $x = 0.35$ and 0.50 leading to $\delta_C^{\text{PM}} = 0.61(3) \text{ mm/s}$ and $\delta_C^{\text{PM}} = 0.60(1) \text{ mm/s}$. For $x = 0.35$, below the onset of the magnetic order, a deviation from the paramagnetic behavior is found. δ_C^{PM} is reduced to a value of $\delta_C^{\text{AFM}} = 0.57(1) \text{ mm/s}$. For $x = 0.50$, a reduction to a value of $\delta_C^{\text{AFM}} = 0.56(1) \text{ mm/s}$ was observed. Also, this reduction occurs over a wider

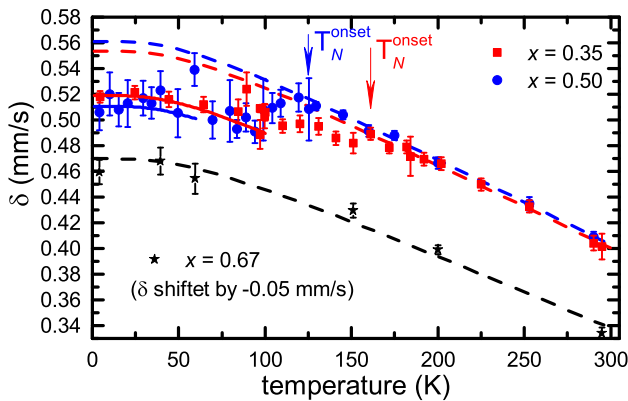


FIG. 11. Temperature dependence of the isomer shift. The dashed (solid) lines are a fit in the paramagnetic (magnetically ordered) temperature regime using Eq. (15) with $\theta_D = 200$ K, 203 K, and 213 K for $x = 0.35$, 0.50, and 0.67, respectively, leading to $\delta^{\text{PM}}(T)$. The deviation from $\delta^{\text{PM}}(T)$ corresponds to the magneto-structural transition, which causes a change in the electron-density at the nucleus. Data and fit for $x = 0.67$ are shifted by $\delta = -0.05$ mm/s for clarity.

temperature range as the magnetic transition is broader. These reductions in the chemical shifts correspond to an increase in the electron density at the nucleus.⁵³ The origin of this increase can be the structural or the magnetic phase transition. The change from a tetragonal to an orthorhombic structure changes the lattice parameters and hence the volume of the unit cell, which may change the chemical shift.⁵³ An increase of the volume and hence an increase of the Fe-As distance results in an decrease of the electron density at the nucleus corresponding to an increased δ_C .⁵⁵ This behavior is for example observed in nonmagnetic FeSe, which shows an increase in δ_C of 0.006(1) mm/s at the tetragonal-to-orthorhombic phase transition.⁵⁶ A magnetic phase transition may change the chemical shift, as observed in metallic iron at the Curie temperature, where no structural phase transition occurs.⁵⁷ The reduction of δ_C in metallic iron due to the magnetic phase transition is ≈ 0.3 mm/s.⁵⁷ This may indicate that the origin of the change of the chemical shifts is of both magnetic and structural nature. However, previous Mössbauer measurements on the undoped compound show contradicting results with either no change,²⁶ an increase⁵⁵, or a decrease⁵⁸ in the chemical shift.

For $x = 0.67$, the temperature dependence of $\delta(T)$ can be properly described by Eq. (15) and a value of $\delta_C = 0.56(1)$ mm/s was obtained. Therefore, no signs of a magnetic or structural phase transition were found.

E. Optimal doped $\text{Ca}_{0.33}\text{Na}_{0.67}\text{Fe}_2\text{As}_2$

For $\text{Ca}_{0.33}\text{Na}_{0.67}\text{Fe}_2\text{As}_2$ ($x = 0.67$), susceptibility measurements evidence bulk superconductivity below

$T_c = 34$ K, as shown in Fig. 2. Mössbauer spectra down to 5 K are shown in Fig. 6. Above 151 K, a doublet structure with $V_{zz} = 10.3(2)$ V/Å² is observed. This is consistent with a pure paramagnetic phase. V_{zz} is constant within error bars down to lowest temperatures indicating the absence of a structural phase transition. Below 60 K, a broadening of the spectra is observed. This broadening indicates small magnetic fields, which were modeled using a Gaussian distribution with a first moment $\langle B \rangle = 0$. The standard deviation of this Gaussian distribution is constant within error bars, $\sigma(B) = 2.2(1)$ T, above T_c and decreases in the superconducting phase to 1.7(1) T at 4.2 K. This indicates a competition between magnetism and superconductivity. Additionally, the spectra are nearly symmetric below 60 K and an angle $\theta = 55(5)^\circ$ between the principal axis of the EFG and the magnetic hyperfine field is obtained, which is close to the magic angle. ZF- μ SR-experiments down to 5 K are shown in Fig. 3. The time evolution of the muon spin polarization exhibits a Gauss-Kubo-Toyabe depolarization above 75 K excluding any electronic magnetic order. Below 40 K, a weak exponential relaxation supports short-range magnetic order in a small volume fraction with a MVF smaller than 20 %. By combining both local probes, the onset temperature of the weak magnetic order is estimated to be $60 \text{ K} < T_N^{\text{onset}} < 75 \text{ K}$. However, room-temperature Mössbauer measurements as well as the sharp superconducting transition observed by magnetic-susceptibility measurements indicate a homogeneous sample. This indicates that the weak magnetism is diluted and disordered and persistent even in the optimal doping regime, similar to other iron pnictides.^{61–63}

For an investigation of the superconducting phase, TF- μ SR measurements were performed in an external magnetic fields of $\mu_0 H_{\text{ext}} = 11.8$ mT perpendicular and parallel to the crystallographic c -axis. The magnetic field was applied at $T > T_c$ and the corresponding muon spin polarization is shown in Fig. 12(a). The weak relaxation above T_c is caused by the dipole-dipole interaction of the muon spin with randomly distributed dense nuclear moments. Additional damping is found in the case of a type-II superconductor for $\mu_0 H_{c1} < \mu_0 H_{\text{ext}} < \mu_0 H_{c2}$ due to the vortex lattice formation. The effect of the vortex lattice on the muon spin polarization is shown in Fig. 12(b)–(d). The superconducting signal fraction is fully damped after a few μs and ≈ 18 % residual signal fraction is still oscillating with a precession frequency equal to the applied field at times $t > 3 \mu\text{s}$. Identifying this ≈ 18 % signal fraction with the MVF obtained by ZF- μ SR measurements, which is of equal value, shows that the internal magnetic fields are small compared to the 11.8 mT applied field.

The London penetration depth can be obtained by measuring the magnetic-field distribution within the vortex lattice and employing Eq. (4). Using the measurements with $\mu_0 H_{\text{ext}} \parallel c$, the in-plane penetration depth λ_{ab} can be directly calculated. For $\mu_0 H_{\text{ext}} \perp c$, contributions from λ_{ac} and λ_{bc} are measured resulting in an

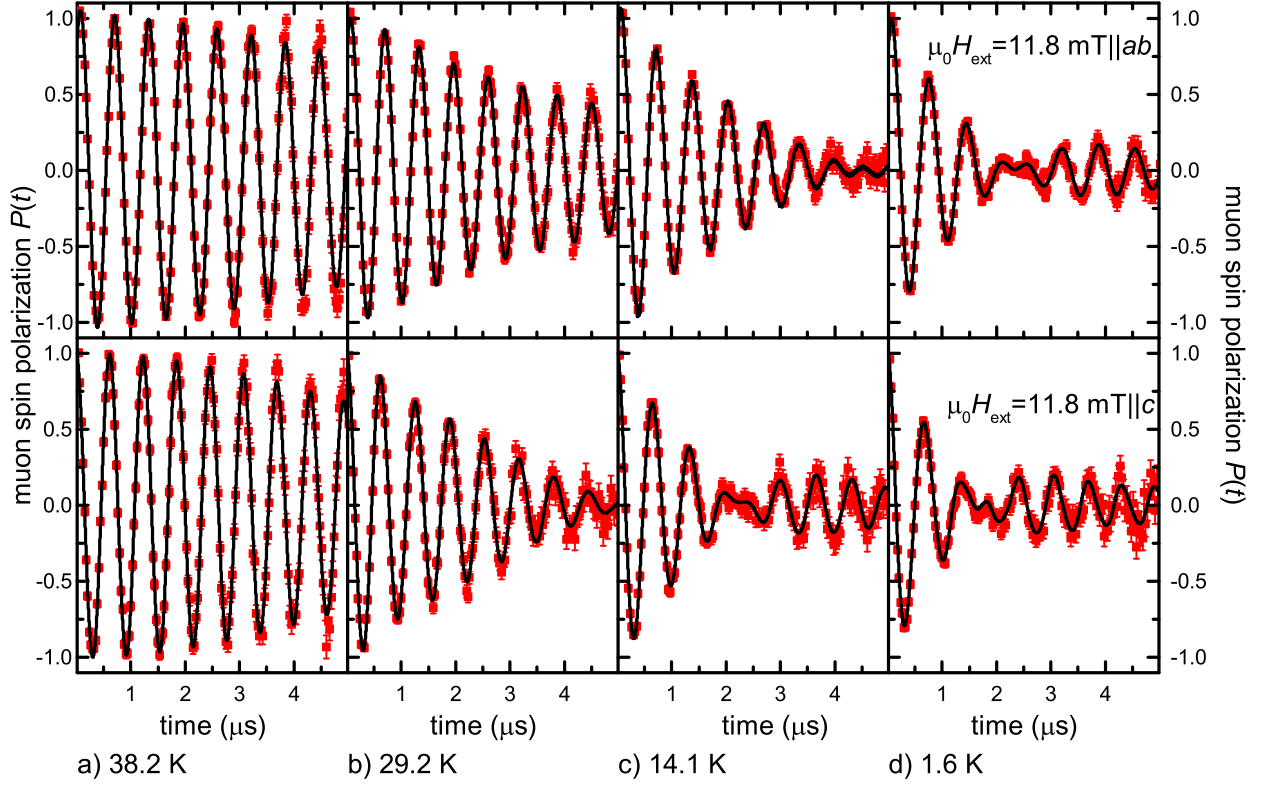


FIG. 12. TF- μ SR spectra for $x = 0.67$ with $\mu_0 H_{\text{ext}} = 11.8 \text{ mT} \parallel ab$ (upper row) and $\mu_0 H_{\text{ext}} = 11.8 \text{ mT} \parallel c$ (lower row) for temperatures above and below the superconducting transition temperature $T_c = 34 \text{ K}$. The small (Gaussian) damping in spectrum (a) is attributed to the dipolar interaction of the muon spin with randomly distributed nuclear moments. The additional damping in spectra (b)–(d) is caused by the formation of the vortex lattice in the superconducting state and the associated internal magnetic field distribution $n(B)$. It is clearly visible that the damping of the muon precession is stronger in the case $\mu_0 H_{\text{ext}} = 11.8 \text{ mT} \parallel c$.

effective magnetic penetration depth λ_{ceff} . Under the assumption of $\lambda_a \approx \lambda_b$, a value for λ_c can be estimated using⁶⁴

$$\lambda_{ab} = \sqrt{\lambda_a \lambda_b} \approx \lambda_a \rightarrow \lambda_{\text{ceff}} = \sqrt{\lambda_a \lambda_c} \rightarrow \lambda_c = \frac{\lambda_{\text{ceff}}^2}{\lambda_a}. \quad (17)$$

The resulting temperature dependence of the inverse squared London penetration depth, $1/\lambda_{ab}^2(T)$ and $1/\lambda_c^2(T)$, is shown in Fig. 13(a) and Fig. 13(b), respectively, together with the average internal field $\langle B \rangle$, which shows a reduction due to the diamagnetic shielding below the superconducting transition. $1/\lambda^2(T)$ was modeled using the phenomenological α -model including two independent superconducting gaps with s -wave symmetry and a fixed $T_c = 34 \text{ K}$.⁵⁹ The results are shown in Tab. II as well as results of ARPES⁶⁵ ($x = 0.67$) and specific-heat measurements⁹ ($x = 0.68$) on single crystals. Disorder in the vortex lattice would artificially reduce the magnetic penetration depth due to the broadening of $n(B)$. Therefore, λ_{ab} and λ_c strictly describe lower limits (and λ^{-2} an upper limit). Therefore,

	$\Delta_1(0)/\text{meV}$	$\Delta_2(0)/\text{meV}$	$W(\Delta_1)$	$\lambda(0)/\text{nm}$
λ_c	0.57(8)	6.7(1.3)	0.49(4)	280(46)
λ_{ab}	0.8(3)	6(1)	0.46(8)	194(17)
ARPES ⁶⁵	2.3	7.8		
spec. heat ^{9,60}	2.35	7.5	0.75 ⁹	210(10) ⁶⁰

TABLE II. Values of the superconducting gap and the magnetic penetration depth obtained by a phenomenological α -model analysis of $1/\lambda_c^2(T)$ and $1/\lambda_{ab}^2(T)$. $\Delta_i(0)$ denotes the zero temperature values of the gaps. $W(\Delta_1)$ and $W(\Delta_2) = 1 - W(\Delta_1)$ are the corresponding weighting factors. $\lambda(0)$ denotes the zero-temperature penetration depth.

the obtained values for the magnetic penetration depths are reduced compared to the values obtained by, e.g., specific-heat measurements. To illustrate this effect, the temperature dependence of $\lambda_{\text{spec. heat}}^{-2}(T)$ with the cor-

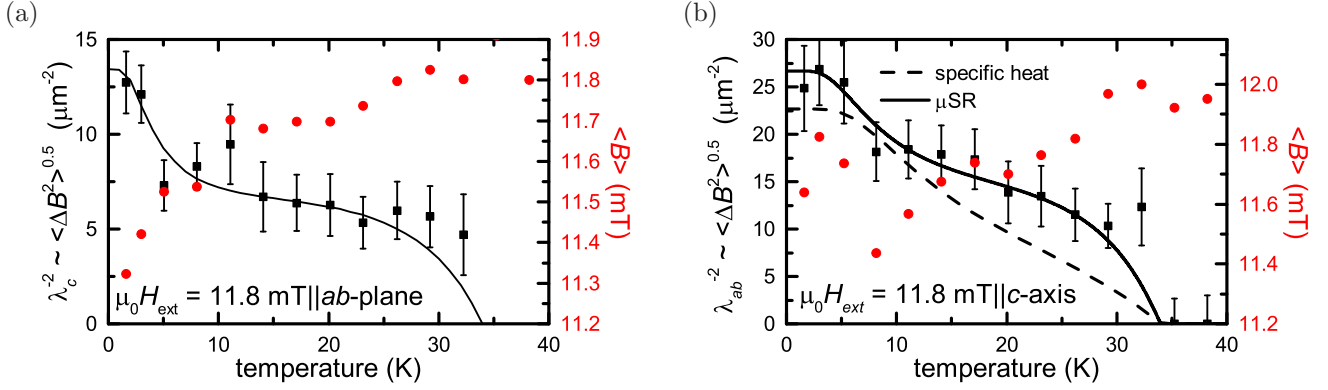


FIG. 13. Temperature dependence of the magnetic penetration depth (a) $\lambda_c^{-2}(T)$ and (b) $\lambda_{ab}^{-2}(T)$ (proportional to the superfluid density) after field cooling in $\mu_0 H = 11.8$ mT, including the fit (solid lines) with a phenomenological α -model,⁵⁹ and the average magnetic field determined by TF- μ SR. The dashed curve in (b) displays the temperature dependence of λ^{-2} with gap values of $\Delta_1 = 2.35$ meV, $\Delta_2 = 7.5$ meV, $W(\Delta_1) = 0.75$, and $\lambda(0) = 210$ nm, obtained by specific-heat measurements^{9,60}. The reduction of the average magnetic field is caused by the diamagnetic shielding of the superconducting phase.

responding parameter ($\Delta_1 = 2.35$ meV, $\Delta_2 = 7.5$ meV, $W(\Delta_1) = 0.75$ and $\lambda(0) = 210$ nm) obtained by specific-heat measurements^{9,60} is plotted in Fig. 13b. It is clearly visible that $\lambda_{\text{spec. heat}}^{-2}(T) < \lambda_{\mu\text{SR}}^{-2}(T)$ for $T < T_c$. This underestimation of the magnetic penetration depth in the μ SR experiments may result in a different temperature dependence of $\lambda^{-2}(T)$ and therefore in different gap sizes and weighting factors. Additionally, Johnston *et al.* considered the interband coupling of the superconducting bands and found an intermediate coupling strength.⁹ The α -model used in this work considers two noninteracting superconducting bands, which may also explain the different parameter values. Nevertheless, taking into account the limitation of magnetic penetration depth measurements by means of μ SR experiments and of the used α -model, the obtained parameter for $\Delta_1(0)$, $\Delta_2(0)$, $W(\Delta_1)$, and $\lambda(0)$ are in good agreement with the values obtained by ARPES and specific heat experiments.^{9,60,65}

The anisotropy of the magnetic penetration can be calculated by under the assumption that $\lambda_a \approx \lambda_b$ by⁶⁴

$$\gamma_\lambda = \frac{\lambda_c}{\lambda_{ab}}. \quad (18)$$

A temperature-independent value of $\gamma_\lambda = 1.5(4)$ is the smallest observed among the 122 pnictides indicating a more 3D-behavior.⁹ This behavior is consistent with the temperature-independent value of $\gamma = 1.85(5)$ for the anisotropy of the upper critical fields.⁶⁶

IV. SUMMARY AND CONCLUSIONS

In summary, we performed muon spin relaxation and Mössbauer experiments on $\text{Ca}_{1-x}\text{Na}_x\text{Fe}_2\text{As}_2$ single crystals with $x = 0.00, 0.35, 0.50$, and 0.67 resulting in an updated phase diagram, which is shown in Fig. 14. The substitution of Ca by Na reduces the onset of the mag-

netic ordering from $T_N^{\text{onset}} = 167(2)$ K to $161(2)$ K and $125(3)$ K while the magnetic phase transition temperature width $\Delta T = T_N^{\text{onset}} - T_N^{100}$ % increases from 4 K to 21 K and 45 K for $x = 0.00, 0.35$, and 0.50 , respectively. The muon spin precession frequency ν as well as the magnetic hyperfine field B_{hf} , which are proportional to the magnetic order parameter, are reduced as a function of the Na-substitution level. Both μ SR as well as Mössbauer spectroscopy indicate an increased tilting of the magnetic structure upon doping. The magnetic phase transition is accompanied by a structural phase transition. The lattice dynamics does not change at the magneto-structural phase transition. Magnetic susceptibility measurements indicate superconductivity in parts of the sample volume for $x = 0.35$, whereas the sample with $x = 0.50$ shows bulk superconductivity. Therefore, as 100% of the sample is magnetically ordered, coexistence of magnetic order and superconductivity in parts ($x = 0.35$) or in the whole sample ($x = 0.50$) was observed. A strong reduction of the magnetic order parameter, as found in the $\text{Ba}_{1-x}\text{Na}_x\text{Fe}_2\text{As}_2$ series,³⁰ is not observed for $\text{Ca}_{1-x}\text{Na}_x\text{Fe}_2\text{As}_2$ with $x = 0.35$. For $x = 0.50$, a small reduction of ≈ 7 % was observed. We applied a Landau theory to describe the reduction of the magnetic order parameter showing that the magnitude of the reduction depends on the coupling strength and the T_c/T_N ratio. A linear relation between the reduction of $|\vec{M}_{\text{co}}|^2/|\vec{M}_0|^2(T=0)$ on T_c/T_N has been found for several superconducting 122-pnictide systems that microscopic coexistence.

For $x = 0.67$, diluted and weak magnetism below 60–75 K as well as bulk superconductivity with $T_c = 34$ K is found. The s -wave symmetry of the two superconducting gaps as well as the value of the larger gap agrees well with recent ARPES- and specific-heat measurements.^{65,67}

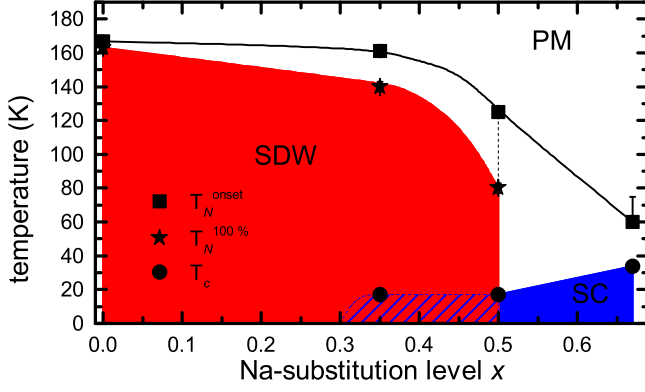


FIG. 14. Updated phase diagram of $\text{Ca}_{1-x}\text{Na}_x\text{Fe}_2\text{As}_2$. The magnetic order is suppressed as a function of the Na-substitution level x . The temperature width of the magnetic phase transition $\Delta T = T_N^{\text{onset}} - T_N^{100\%}$ increases as a function of x due to the enhanced degree of disorder due to the Na substitution. For $x = 0.35, 0.50$, and 0.67 nanoscopic coexistence of magnetic order and superconductivity is found below T_c .

ACKNOWLEDGMENTS

This work was funded by the German Science Foundation (DFG) within the research training group GRK 1621 as well as under the Projects WU595/3-1 (S. W.), BE1749/13 and BU887/15-1 (B. B.), and SA 2426/1-1 (R. S.). Part of this work was performed at the Swiss Muon Source at the Paul Scherrer Institute, Switzerland.

- ¹ Y. Kamihara, T. Watanabe, M. Hirano, and H. Hosono, *Journal of the American Chemical Society* **130**, 3296 (2008).
- ² J. Schmiedt, P. M. R. Brydon, and C. Timm, *Phys. Rev. B* **89**, 054515 (2014).
- ³ D. Parker, M. G. Vavilov, A. V. Chubukov, and I. I. Mazin, *Phys. Rev. B* **80**, 100508 (2009).
- ⁴ R. M. Fernandes and J. Schmalian, *Phys. Rev. B* **82**, 014521 (2010).
- ⁵ A. B. Vorontsov, M. G. Vavilov, and A. V. Chubukov, *Phys. Rev. B* **81**, 174538 (2010).
- ⁶ R. M. Fernandes, D. K. Pratt, W. Tian, J. Zarestky, A. Kreyssig, S. Nandi, M. G. Kim, A. Thaler, N. Ni, P. C. Canfield, R. J. McQueeney, J. Schmalian, and A. I. Goldman, *Phys. Rev. B* **81**, 140501 (2010).
- ⁷ K. Zhao, Q. Q. Liu, X. C. Wang, Z. Deng, Y. X. Lv, J. L. Zhu, F. Y. Li, and C. Q. Jin, *Phys. Rev. B* **84**, 184534 (2011).
- ⁸ G. Wu, H. Chen, T. Wu, Y. L. Xie, Y. J. Yan, R. H. Liu, X. F. Wang, J. J. Ying, and X. H. Chen, *Journal of Physics: Condensed Matter* **20**, 422201 (2008).
- ⁹ S. Johnston, M. Abdel-Hafez, L. Harnagea, V. Grinenko, D. Bombor, Y. Krupskaya, C. Hess, S. Wurmehl, A. U. B. Wolter, B. Büchner, H. Rosner, and S.-L. Drechsler, *Phys. Rev. B* **89**, 134507 (2014).
- ¹⁰ A. Suter and B. Wojek, *Physics Procedia* **30**, 69 (2012).
- ¹¹ P. D. de Rotier and A. Yaouanc, *Journal of Physics: Condensed Matter* **9**, 9113 (1997).
- ¹² A. Yaouanc and P. de Réotier, *Muon Spin Rotation, Relaxation, and Resonance: Applications to Condensed Matter*, International Series of Monographs on Physics (OUP Oxford, 2011).
- ¹³ A. Maisuradze, R. Khasanov, A. Shengelaya, and H. Keller, *Journal of Physics: Condensed Matter* **21**, 075701 (2009).
- ¹⁴ E. H. Brandt, *Phys. Rev. B* **37**, 2349 (1988).
- ¹⁵ L. Harnagea, S. Singh, G. Friemel, N. Leps, D. Bombor, M. Abdel-Hafez, A. U. B. Wolter, C. Hess, R. Klingeler, G. Behr, S. Wurmehl, and B. Büchner, *Phys. Rev. B* **83**, 094523 (2011).
- ¹⁶ S. Aswartham, M. Abdel-Hafez, D. Bombor, M. Kumar, A. U. B. Wolter, C. Hess, D. V. Evtushinsky, V. B. Zabolotnyy, A. A. Kordyuk, T. K. Kim, S. V. Borisenko, G. Behr, B. Büchner, and S. Wurmehl, *Phys. Rev. B* **85**, 224520 (2012).
- ¹⁷ R. Klingeler, N. Leps, I. Hellmann, A. Popa, U. Stockert, C. Hess, V. Kataev, H.-J. Grafe, F. Hammerath, G. Lang, S. Wurmehl, G. Behr, L. Harnagea, S. Singh, and B. Büchner, *Phys. Rev. B* **81**, 024506 (2010).
- ¹⁸ G. M. Zhang, Y. H. Su, Z. Y. Lu, Z. Y. Weng, D. H. Lee, and T. Xiang, *EPL (Europhysics Letters)* **86**, 37006 (2009).
- ¹⁹ A. A. Aczel, E. Baggio-Saitovitch, S. L. Budko, P. C. Canfield, J. P. Carlo, G. F. Chen, P. Dai, T. Goko, W. Z. Hu, G. M. Luke, J. L. Luo, N. Ni, D. R. Sanchez-Candela, F. F. Tafti, N. L. Wang, T. J. Williams, W. Yu, and Y. J. Uemura, *Phys. Rev. B* **78**, 214503 (2008).
- ²⁰ A. Jesche, N. Caroca-Canales, H. Rosner, H. Borrmann, A. Ormeci, D. Kasinathan, H. H. Klauss, H. Luetkens, R. Khasanov, A. Amato, A. Hoser, K. Kaneko, C. Krellner, and C. Geibel, *Phys. Rev. B* **78**, 180504 (2008).
- ²¹ H.-H. Klauss, H. Luetkens, R. Klingeler, C. Hess, F. J. Litterst, M. Kraken, M. M. Korshunov, I. Eremin, S.-L. Drechsler, R. Khasanov, A. Amato, J. Hamann-Borrero, N. Leps, and G. Behr, *Phys. Rev. Lett.* **101**, 077005 (2008).
- ²² A. Amato, R. Khasanov, H. Luetkens, and H.-H. Klauss, *Physica C: Superconductivity* **469**, 606 (2009), superconductivity in Iron-Pnictides.
- ²³ E. Wiesenmayer, H. Luetkens, G. Pascua, R. Khasanov, A. Amato, H. Potts, B. Banusch, H.-H. Klauss, and D. Johrendt, *Phys. Rev. Lett.* **107**, 237001 (2011).

- ²⁴ R. D. Shannon, *Acta Crystallographica Section A* **32**, 751 (1976).
- ²⁵ M. Rotter, M. Pangerl, M. Tegel, and D. Johrendt, *Angewandte Chemie International Edition* **47**, 7949 (2008).
- ²⁶ M. Alzamora, J. Munevar, E. Baggio-Saitovitch, S. L. Budko, N. Ni, P. C. Canfield, and D. R. Sanchez, *Journal of Physics: Condensed Matter* **23**, 145701 (2011).
- ²⁷ A. I. Goldman, D. N. Argyriou, B. Ouladdiaf, T. Chatterji, A. Kreyssig, S. Nandi, N. Ni, S. L. Bud'ko, P. C. Canfield, and R. J. McQueeney, *Phys. Rev. B* **78**, 100506 (2008).
- ²⁸ D. Kasinathan, A. Ormeci, K. Koch, U. Burkhardt, W. Schnelle, A. Leithe-Jasper, and H. Rosner, *New Journal of Physics* **11**, 025023 (2009).
- ²⁹ Q. Huang, Y. Qiu, W. Bao, M. A. Green, J. W. Lynn, Y. C. Gasparovic, T. Wu, G. Wu, and X. H. Chen, *Phys. Rev. Lett.* **101**, 257003 (2008).
- ³⁰ H. Maeter, G. Pascua, H. Luetkens, J. Knolle, S. Aswartham, S. Wurmehl, G. Behr, B. Büchner, Z. Shermadini, K. Sedlak, A. Amato, R. Moessner, I. Eremin, and H.-H. Klauss, *arXiv* **1210.6881v1** (2012).
- ³¹ T. Goko, A. A. Aczel, E. Baggio-Saitovitch, S. L. Bud'ko, P. C. Canfield, J. P. Carlo, G. F. Chen, P. Dai, A. C. Hamann, W. Z. Hu, H. Kageyama, G. M. Luke, J. L. Luo, B. Nachumi, N. Ni, D. Reznik, D. R. Sanchez-Candela, A. T. Savici, K. J. Sikes, N. L. Wang, C. R. Wiebe, T. J. Williams, T. Yamamoto, W. Yu, and Y. J. Uemura, *Phys. Rev. B* **80**, 024508 (2009).
- ³² S. Avci, J. M. Allred, O. Chmaissem, D. Y. Chung, S. Rosenkranz, J. A. Schlueter, H. Claus, A. Daoud-Aladine, D. D. Khalyavin, P. Manuel, A. Lobet, M. R. Suchomel, M. G. Kanatzidis, and R. Osborn, *Phys. Rev. B* **88**, 094510 (2013).
- ³³ R. Cortes-Gil and S. J. Clarke, *Chemistry of Materials* **23**, 1009 (2011), <http://dx.doi.org/10.1021/cm1028244>.
- ³⁴ H. Suhl, *Journal of the Less Common Metals* **62**, 225 (1978).
- ³⁵ T. K. Kopec and J. Klamut, *physica status solidi (b)* **137**, 73 (1986).
- ³⁶ M. G. Vavilov, A. V. Chubukov, and A. B. Vorontsov, *Superconductor Science and Technology* **23**, 054011 (2010).
- ³⁷ C. R. Rotundu, W. Tian, K. C. Rule, T. R. Forrest, J. Zhao, J. L. Zarestky, and R. J. Birgeneau, *Phys. Rev. B* **85**, 144506 (2012).
- ³⁸ S. Avci, O. Chmaissem, E. A. Goremychkin, S. Rosenkranz, J.-P. Castellan, D. Y. Chung, I. S. Todorov, J. A. Schlueter, H. Claus, M. G. Kanatzidis, A. Daoud-Aladine, D. Khalyavin, and R. Osborn, *Phys. Rev. B* **83**, 172503 (2011).
- ³⁹ M. G. Kim, D. K. Pratt, G. E. Rustan, W. Tian, J. L. Zarestky, A. Thaler, S. L. Bud'ko, P. C. Canfield, R. J. McQueeney, A. Kreyssig, and A. I. Goldman, *Phys. Rev. B* **83**, 054514 (2011).
- ⁴⁰ A. Kreyssig, M. G. Kim, S. Nandi, D. K. Pratt, W. Tian, J. L. Zarestky, N. Ni, A. Thaler, S. L. Bud'ko, P. C. Canfield, R. J. McQueeney, and A. I. Goldman, *Phys. Rev. B* **81**, 134512 (2010).
- ⁴¹ P. Wang, Z. M. Stadnik, J. Zukrowski, A. Thaler, S. L. Bud'ko, and P. C. Canfield, *Phys. Rev. B* **84**, 024509 (2011).
- ⁴² H. Luo, R. Zhang, M. Laver, Z. Yamani, M. Wang, X. Lu, M. Wang, Y. Chen, S. Li, S. Chang, J. W. Lynn, and P. Dai, *Phys. Rev. Lett.* **108**, 247002 (2012).
- ⁴³ S. Nandi, M. G. Kim, A. Kreyssig, R. M. Fernandes, D. K. Pratt, A. Thaler, N. Ni, S. L. Bud'ko, P. C. Canfield, J. Schmalian, R. J. McQueeney, and A. I. Goldman, *Phys. Rev. Lett.* **104**, 057006 (2010).
- ⁴⁴ P. Marsik, K. W. Kim, A. Dubroka, M. Rössle, V. K. Malik, L. Schulz, C. N. Wang, C. Niedermayer, A. J. Drew, M. Willis, T. Wolf, and C. Bernhard, *Phys. Rev. Lett.* **105**, 057001 (2010).
- ⁴⁵ A. D. Christianson, M. D. Lumsden, S. E. Nagler, G. J. MacDougall, M. A. McGuire, A. S. Sefat, R. Jin, B. C. Sales, and D. Mandrus, *Phys. Rev. Lett.* **103**, 087002 (2009).
- ⁴⁶ D. K. Pratt, M. G. Kim, A. Kreyssig, Y. B. Lee, G. S. Tucker, A. Thaler, W. Tian, J. L. Zarestky, S. L. Bud'ko, P. C. Canfield, B. N. Harmon, A. I. Goldman, and R. J. McQueeney, *Phys. Rev. Lett.* **106**, 257001 (2011).
- ⁴⁷ T. Goltz, V. Zinth, D. Johrendt, H. Rosner, G. Pascua, H. Luetkens, P. Materne, and H.-H. Klauss, *Phys. Rev. B* **89**, 144511 (2014).
- ⁴⁸ T. Yildirim, *Physica C: Superconductivity* **469**, 425 (2009), superconductivity in Iron-Pnictides.
- ⁴⁹ S. E. Hahn, Y. Lee, N. Ni, P. C. Canfield, A. I. Goldman, R. J. McQueeney, B. N. Harmon, A. Alatas, B. M. Leu, E. E. Alp, D. Y. Chung, I. S. Todorov, and M. G. Kanatzidis, *Phys. Rev. B* **79**, 220511 (2009).
- ⁵⁰ R. Mittal, S. K. Mishra, S. L. Chaplot, S. V. Ovsyannikov, E. Greenberg, D. M. Trots, L. Dubrovinsky, Y. Su, T. Brueckel, S. Matsuishi, H. Hosono, and G. Garbarino, *Phys. Rev. B* **83**, 054503 (2011).
- ⁵¹ L. Chauvière, Y. Gallais, M. Cazayous, A. Sacuto, M. A. Méasson, D. Colson, and A. Forget, *Phys. Rev. B* **80**, 094504 (2009).
- ⁵² R. Housley, N. Erickson, and J. Dash, *Nuclear Instruments and Methods* **27**, 29 (1964).
- ⁵³ D. Barb, *Grundlagen und Anwendungen der Mössbauerspektroskopie* (Berlin, Akademie-Verlag, 1980).
- ⁵⁴ G. Lang, *Nuclear Instruments and Methods* **24**, 425 (1963).
- ⁵⁵ Z. Li, X. Ma, H. Pang, and F. Li, *Journal of Physics: Condensed Matter* **23**, 255701 (2011).
- ⁵⁶ A. Blachowski, K. Ruebenbauer, J. Zukrowski, J. Przewonik, K. Wojciechowski, and Z. Stadnik, *Journal of Alloys and Compounds* **494**, 1 (2010).
- ⁵⁷ R. S. Preston, *Phys. Rev. Lett.* **19**, 75 (1967).
- ⁵⁸ A. Blachowski, K. Ruebenbauer, J. Zukrowski, K. Rogacki, Z. Bukowski, and J. Karpinski, *Phys. Rev. B* **83**, 134410 (2011).
- ⁵⁹ A. Carrington and F. Manzano, *Physica C: Superconductivity* **385**, 205 (2003).
- ⁶⁰ M. Abdel-Hafez, P. J. Pereira, S. A. Kuzmichev, T. E. Kuzmicheva, V. M. Pudalov, L. Harnagea, A. A. Kordyuk, A. V. Silhanek, V. V. Moshchalkov, B. Shen, H.-H. Wen, A. N. Vasiliev, and X.-J. Chen, *Phys. Rev. B* **90**, 054524 (2014).
- ⁶¹ C. Bernhard, A. J. Drew, L. Schulz, V. K. Malik, M. Rössle, C. Niedermayer, T. Wolf, G. D. Varma, G. Mu, H.-H. Wen, H. Liu, G. Wu, and X. H. Chen, *New Journal of Physics* **11**, 055050 (2009).
- ⁶² A. J. Drew, C. Niedermayer, P. J. Baker, F. L. Pratt, S. J. Blundell, T. Lancaster, R. H. Liu, G. Wu, X. H. Chen, I. Watanabe, V. K. Malik, A. Dubroka, M. Rössle, K. W. Kim, C. Baines, and C. Bernhard, *Nat Mater* **8**, 310 (2009).
- ⁶³ H. Luetkens, H.-H. Klauss, M. Kraken, F. J. Litterst, T. Dellmann, R. Klingeler, C. Hess, R. Khasanov, A. Amato, C. Baines, M. Kosmala, O. J. Schumann, M. Braden, J. Hamann-Borrero, N. Leps, A. Kondrat, G. Behr, J. Werner, and B. Buchner, *Nat Mater* **8**, 305 (2009).

- ⁶⁴ R. Khasanov, D. Evtushinsky, A. Amato, H.-H. Klauss, H. Luetkens, C. Niedermayer, B. Büchner, G. Sun, C. Lin, J. Park, D. Inosov, and V. Hinkov, Phys. Rev. Lett. **102**, 187005 (2009).
- ⁶⁵ D. V. Evtushinsky, V. B. Zabolotnyy, L. Harnagea, A. N. Yaresko, S. Thirupathaiah, A. A. Kordyuk, J. Maletz, S. Aswartham, S. Wurmehl, E. Rienks, R. Follath, B. Büchner, and S. V. Borisenko, Phys. Rev. B **87**, 094501 (2013).
- ⁶⁶ N. Haberkorn, B. Maierov, M. Jaime, I. Usov, M. Miura, G. F. Chen, W. Yu, and L. Civale, Phys. Rev. B **84**, 064533 (2011).
- ⁶⁷ Y.-B. Shi, Y.-B. Huang, X.-P. Wang, X. Shi, A. van Roekeghem, W.-L. Zhang, N. Xu, P. Richard, T. Qian, E. Rienks, S. Thirupathaiah, K. Zhao, C.-Q. Jin, M. Shie, and H. Ding, arXiv **1402.5875** (2014).